



OPEN

## Construction of chitosan-supported nickel cobaltite composite for efficient electrochemical capacitor and water-splitting applications

Shymaa S. Medany<sup>1</sup>✉, Ayman Nafady<sup>2</sup>, Razium Ali Soomro<sup>3</sup> & Mahmoud A. Hefnawy<sup>1</sup>✉

The construction of highly efficient electrode material is of considerable interest, particularly for high capacitance and water-splitting applications. Herein, we present the preparation of a NiCo<sub>2</sub>O<sub>4</sub>-Chitosan (NC@Chit) nanocomposite using a simple hydrothermal technique designed for applications in high capacitance and water-splitting. The structure/composition of the NC@Chit composite was characterized using different analytical methods, containing electron microscope (SEM and TEM), and powder X-ray diffraction (XRD). When configured as an anode material, the NC@Chit displayed a high capacitance of 234 and 345 F g<sup>-1</sup> (@1Ag<sup>-1</sup> for GC/NC and NC@Chit, respectively) in an alkaline electrolyte. The direct use of the catalyst in electrocatalytic water-splitting i.e., HER and OER achieved an overpotential of 240 mV and 310 mV at a current density of 10 mA cm<sup>-2</sup>, respectively. The obtained Tafel slopes for OER and HER were 62 and 71 mV dec<sup>-1</sup>, respectively whereas the stability and durability of the fabricated electrodes were assessed through prolonged chronoamperometry measurement at constant for 10 h. The electrochemical water splitting was studied for modified nickel cobaltite surface using an impedance tool, and the charge transfer resistances were utilized to estimate the electrode activity.

Population expansion and socioeconomic advancement have contributed to a sharp rise in the world's energy demands. Nevertheless, the excessive reliance on conventional fossil fuels has resulted in rapid resource depletion and environmental contamination challenges<sup>1,2</sup>. Creating innovative, clean, and renewable energy sources is highly desirable. The advantages of hydrogen energy, such as its cleanliness, sustainability, and high energy density, are well-established<sup>3-6</sup>. Water electrolysis, as a method for hydrogen production, is particularly noteworthy for its potential to yield high-purity hydrogen, with no carbon emissions and environmental friendliness<sup>7-9</sup>. In the context of catalysts, the abundance of materials, low cost of synthesis, and advantageous catalytic characteristics of transition-metal-based (TM-based) catalysts have drawn much attention than many types of catalysts<sup>10-14</sup>. Currently, platinum (Pt) or Pt-based materials remain the most effective electrocatalysts for the hydrogen evolution reaction (HER) due to their suitable adsorption energy with intermediates. However, their widespread implementation is hindered by their high cost and scarcity, as evidenced by previous research<sup>15-17</sup>. While effective electrocatalysts have traditionally been synthesized using precious metals like Pt, Ir, and Ru, recent advancements have introduced alternatives based on non-noble and earth-abundant metals (such as metal alloys<sup>18,19</sup>, metal carbides, and nitrides<sup>20</sup>, and molecular metal complexes<sup>21</sup>). For energy-related devices, nickel, its alloys (NiCo<sup>18,22</sup>, NiMo<sup>23</sup>, NiFe<sup>24-26</sup>, and NiMn<sup>27,28</sup>), or the equivalent metal oxides represent a promising family of non-precious metal catalysts.

The chemical composition of XY<sub>2</sub>O<sub>4</sub> characterizes metal oxides with a spinel structure where Y represents a trivalent metal ion at the octahedral position, and X represents a divalent metal ion at the tetrahedral position, while oxygen anions are arranged in a close-packed cubic lattice<sup>29</sup>. Until now, c spinel oxides materials such as

<sup>1</sup>Chemistry Department, Faculty of Science, Cairo University, 12613, Giza, Egypt. <sup>2</sup>Department of Chemistry, College of Science, King Saud University, 11451 Riyadh, Saudi Arabia. <sup>3</sup>State Key Laboratory of Chemical Resource Engineering School of Chemistry, Beijing Advanced Innovation Center for Soft Matter Science and Engineering, Beijing 100029, People's Republic of China. ✉email: shymaasamir80@cu.edu.eg; shymaa@sci.cu.edu.eg; maahefnawy@gmail.com; maadel@cu.edu.eg

$\text{CuBi}_2\text{O}_4$ <sup>30</sup>,  $\text{CuFe}_2\text{O}_4$ <sup>31</sup>,  $\text{ZnFe}_2\text{O}_4$ <sup>32</sup>, and  $\text{NiCo}_2\text{O}_4$ <sup>33,34</sup> have been explored for their structure–activity relationship garnering significant attention to water splitting application.

At present, the predominant electrode materials utilized in commercial supercapacitors consist of electric double-layer capacitive materials primarily composed of pure carbon<sup>35,36</sup>. Typically, these devices exhibit favorable cycle longevity and notable maximum power density. However, their specific capacitance and energy density must meet the escalating demand for peak-power augmentation in electric vehicles<sup>37</sup>. When comparing pseudocapacitive materials to pure carbon-based materials, it becomes evident that the former can significantly augment supercapacitors' specific capacitance and energy density. This enhancement is achieved through the utilization of interfacial reversible faradaic reactions as a means to store energy<sup>38</sup>. Furthermore, integrating pseudocapacitive materials with electric double-layer capacitive materials in constructing asymmetric supercapacitors can lead to an additional improvement in the energy and power density of these supercapacitors<sup>39,40</sup>. Traditional pseudocapacitive materials primarily consist of common transitional metal oxides/hydroxides, such as ruthenium dioxide ( $\text{RuO}_2$ ), manganese dioxide ( $\text{MnO}_2$ ), nickel oxide ( $\text{NiO}$ ), nickel hydroxide ( $\text{Ni(OH)}_2$ ), cobalt oxide ( $\text{Co}_3\text{O}_4$ ), cobalt hydroxide ( $\text{Co(OH)}_2$ ), iron oxide ( $\text{Fe}_3\text{O}_4$ ), and their binary counterparts<sup>41–44</sup>.

$\text{NiCo}_2\text{O}_4$ , among various metal oxides, exhibits advantageous characteristics such as affordability, minimal toxicity, and widespread availability. Additionally, the  $\text{NiCo}_2\text{O}_4$  could be hybridized with variety of diverse materials to achieve enhanced supercapacitive properties<sup>45,46</sup>.

In this study, a composite of nickel cobaltite was synthesized using a hydrothermal technique. The resulting modified glassy carbon electrode, with the nickel cobaltite-chitosan composite (GC/NC@Chit), was utilized for both capacitance and water-splitting applications (see Fig. 1). The prepared materials were characterized using several analytical techniques, while electrochemical techniques such as galvanostatic charging/discharging (GCD), and electrochemical impedance (EIS) were used to measure capacitance behavior. The activity of the electrodes toward water splitting was investigated using voltammetry, constant potential chronoamperometry, and constant current potentiometry.

## Experimental section

### Preparation of nickel cobaltite

All chemicals utilized in the study were commercially available and employed without further modification. During the standard synthesis process, urea (3.1 g),  $\text{Ni(CH}_3\text{COO)}_2 \cdot 4\text{H}_2\text{O}$ , and  $\text{Co(CH}_3\text{COO)}_2 \cdot 4\text{H}_2\text{O}$  were added to the solution, with a combined weight of nickel and cobalt acetates amounting to 1.28 g (approximately 4.40 mmol). The solution was agitated for an additional duration of 20 min. Subsequently, the solution was introduced into a stainless-steel autoclave lined with Teflon and subjected to a temperature of 150 °C for 6 h. Upon cooling the autoclave to ambient temperature, the precursor underwent filtration and was subjected to a thorough washing with deionized water, followed by drying in an oven. Subsequently, the desiccated specimens underwent a calcination process at a temperature of 500 °C for 3 h without any inert gas<sup>47</sup>.

### Preparation of nickel cobaltite-supported chitosan (NC@Chit)

NC@Chit composite was produced by homogenizing chitosan with nickel cobaltite nanoparticles as follows: In a standard procedure, 0.5 g of chitosan was placed in a 250 mL beaker, and the temperature was gradually increased with continuous stirring. Subsequently, 0.5 g of  $\text{NiCo}_2\text{O}_4$  was added to the mixture. The solution temperature was then lowered to room temperature. The addition of nickel cobaltite to the chitosan solution led to the bridging

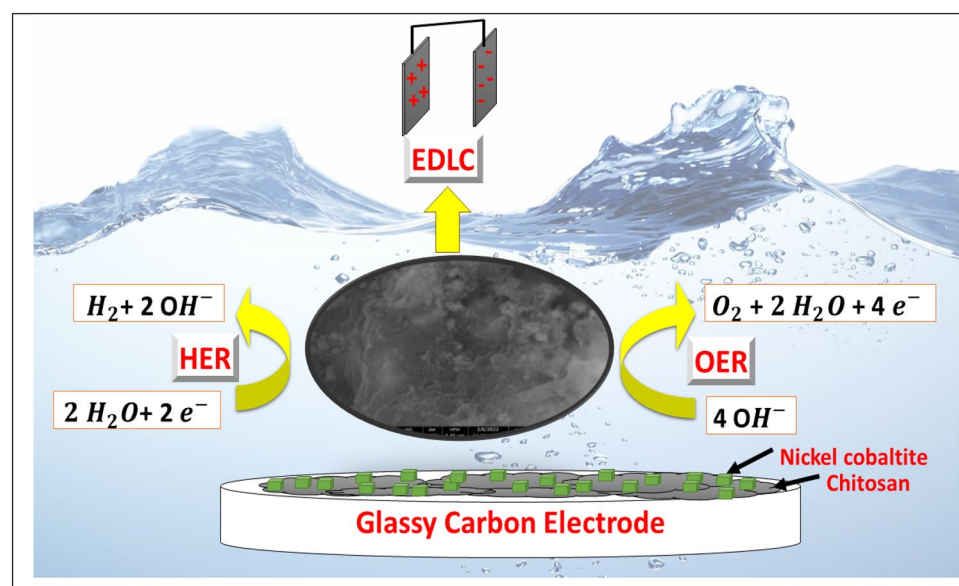


**Figure 1.** Illustration of modified glassy carbon surface for different energy storage applications.

and encapsulation of nickel cobaltite nanoparticles. To achieve a thick consistency, 1 mL of 10% acetic acid was introduced into the mixture and agitated until the desired solution consistency was attained. Following a duration of 10 min, the liquid was filtrated and subsequently rinsed with double distilled water. The product was dried at 60 °C overnight before using as a catalyst.

### Electrode preparation

The working electrode employed in the experiment was a glassy carbon electrode with a 3 mm diameter corresponding to an area of 0.0707 cm<sup>2</sup>. Initially, the surface underwent a polishing process utilizing a delicate emery paper, followed by a thorough cleansing procedure involving ethanol and isopropanol. The casting suspension was prepared by suspended 10 mg of the electrocatalyst powder (NC or NC@Chit) in a mixture of 250 μL of ethanol with 250 μL of 5 wt% Nafion sonicated for 30 min. The electrode was constructed following the deposition of 40 μL catalyst ink onto the GCE surface followed by drying at 50 °C for 4 h. The electrochemical experiments were conducted using the Autolab PGSTAT128N instrument, and the NOVA software facilitated the impedance spectrum analysis. The setup included an Ag/AgCl/KCl (sat.) reference electrode and Pt wire as the counter electrode. The working electrodes employed in the experiment were GC/NC and GC/NC@Chit. For error bar, the data was repeated three times to find out standard error. All potential values were referenced against Ag/AgCl/sat KCl, and for hydrogen evolution reaction (HER) applications, the potential was corrected to the reversible hydrogen electrode (RHE). The potential was determined with respect to the reversible hydrogen electrode (RHE) in relation to the subsequent equations<sup>48</sup>:

$$E_{\text{RHE}} = E_{\text{Ag/AgCl}} + E_{\text{Ag/AgCl}}^{\circ} + 0.059 \text{ pH} \quad (1)$$

The electrochemical experiments were conducted in 1.0 M solution of KOH as the supporting electrolyte. The potential was standardized by employing a reversible hydrogen electrode.

$$E_{\text{RHE}} = E_{\text{Ag/AgCl}} + 1.023(1.0 \text{ M NaOH} \sim \text{pH} = 14) \& \left( E_{\text{Ag/AgCl}}^{\circ} = 0.197 \text{ V} \right) \quad (2)$$

## Result and discussion

### Structure and surface analyses

The chemical structure of prepared chitosan-based nickel cobaltite was characterized using powder X-ray diffraction. Figure 2 shows the X-ray diffraction (XRD) pattern with diffraction peaks for crystalline NC@Chit referenced against amorphous peaks of m-C (JCPDS no. 20-0781)<sup>49</sup> confirming the spinel NiCo<sub>2</sub>O<sub>4</sub> structure with hkl planes of 220, 311, 400, 511, 440, and 533 for peaks at 2θ equal to 30.4, 36.5, 44.1, 58.1, 65.2, and 76.1, respectively. The hump observed at 2θ ~ 12.6 was attributed to the chitosan sheets<sup>50,51</sup>.

The observed peak intensity in the sample containing chitosan decreased, attributed to the presence of embedded nanoparticles within the chitosan sheets. The interaction between chitosan and nickel cobaltite resulted in a modification of the lattice structure<sup>52–54</sup>. To comprehensively understand the molecular-level processes, XRD pattern of NiCo<sub>2</sub>O<sub>4</sub> was referenced against standard peaks of NiCo<sub>2</sub>O<sub>4</sub> crystal as illustrated in Fig. 2. The close match between the theoretical and experimental XRD results confirmed the high quality of the prepared modified NiCo<sub>2</sub>O<sub>4</sub> material using Material studio software.

Scanning electron microscopy (SEM) was utilized to examine the morphological characteristics of the nickel cobaltite nanoparticles, as depicted in Fig. 3a. The particles exhibited a size distribution within the 35–80 nm range. The diminutive size of nickel cobaltite particles suggested an augmented activity level in the synthesized substances. The incorporation of nickel cobaltite into the chitosan sheets is illustrated in Fig. 3a, showcasing

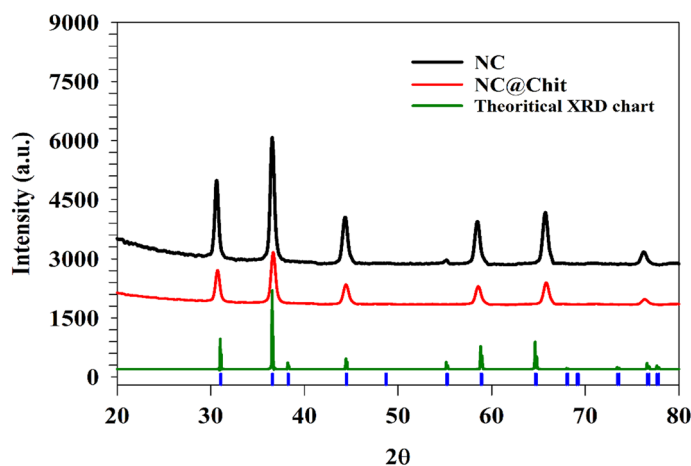


**Figure 2.** XRD pattern of NC@Chit samples referenced against standard peaks of NiCo<sub>2</sub>O<sub>4</sub> crystal.

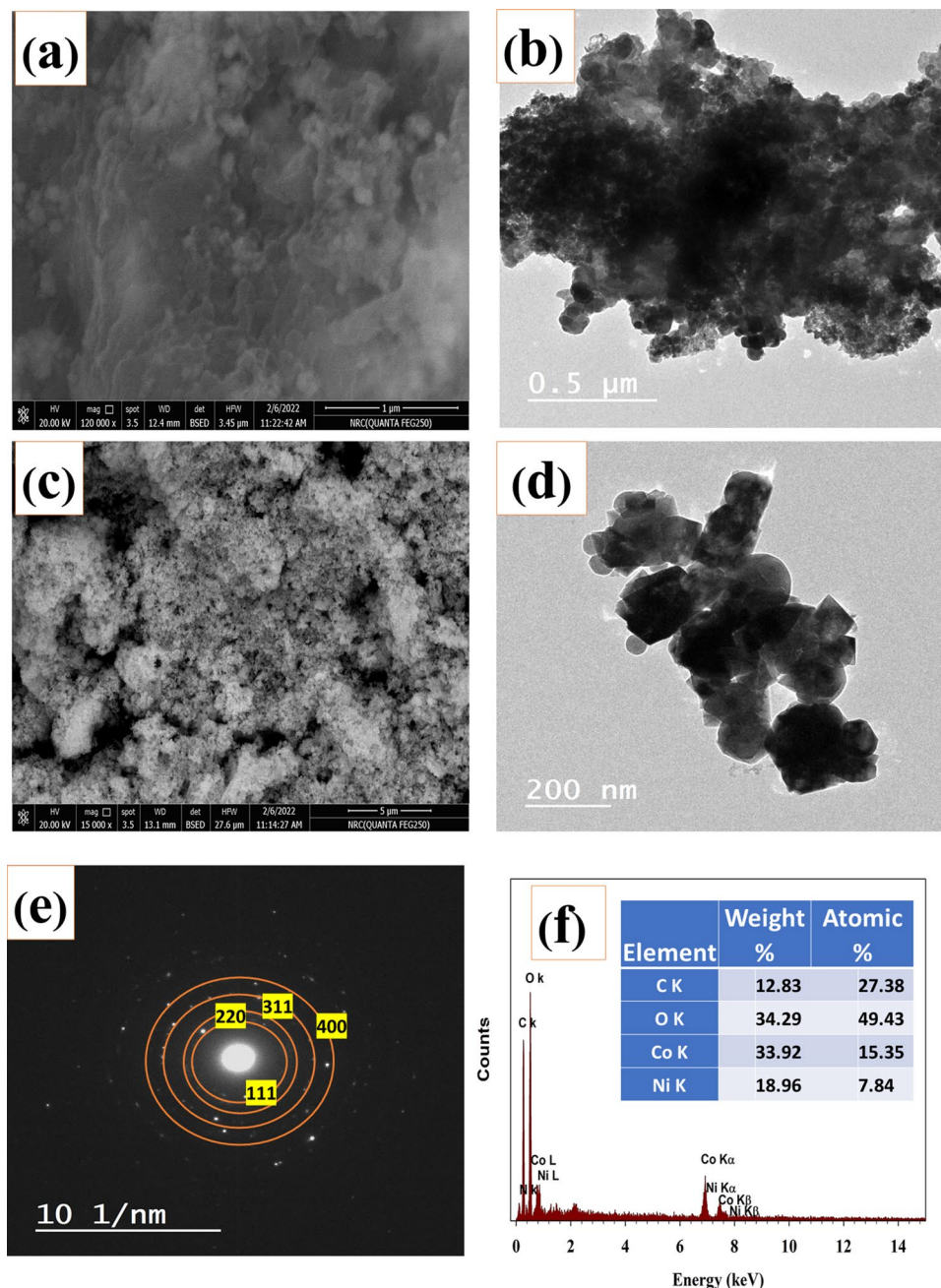


**Figure 3.** Surface characterization of NC@Chit sample by (a) SEM of Chitosan modified NiCo<sub>2</sub>O<sub>4</sub>, (b) TEM Chitosan modified NiCo<sub>2</sub>O<sub>4</sub>, (c) SEM of pristine NiCo<sub>2</sub>O<sub>4</sub>, (d) TEM of pristine NiCo<sub>2</sub>O<sub>4</sub>, (e) diffraction, (f) EDX spectrum.

well-distributed nickel cobaltite particles on the chitosan sheets. Furthermore, the inclusion of chitosan has been observed to enhance water splitting, a phenomenon confirmed by subsequent electrochemical experiments.

Additionally, TEM was employed to determine the morphology of nickel cobaltite nanoparticles. Figure 3b shows the TEM images of NC@Chit composites with mean particle diameter estimated to be around 20–50 nm. The study unveiled that the nanospheres composed of NiCo<sub>2</sub>O<sub>4</sub> exhibited attachment to the chitosan sheets. The presence of NC on the chitosan sheet is validated by utilizing the corresponding transmission electron microscopy (TEM) diffraction patterns. For comparison, pristine nickel cobaltite was characterized using SEM, as depicted in Fig. 3c, revealing nanoparticles with a particle size of approximately 30 nm. Additionally, the TEM of pristine nickel cobaltite was employed in Fig. 3d, highlighting the cubic structure of the particles. The Miller indices (Fig. 3e) from the observed SEAD pattern represents (400), (311), (220), and (111) planes, respectively whereas the EDX spectra confirmed the of Ni, Co, O, C, and N elements as major constituents of NC@Chit

(Fig. 3f). The elemental proportions depicted in the inset figure correspond to the intended composition of NC, wherein the ratio of Ni to Co is 1:2.

### Electrochemical capacitor

Cyclic voltammetry (CV) was employed to assess the activity of modified GC/NC and GC/NC@Chit in a 1.0 M KOH solution. The activation process, a pivotal step in water-splitting reactions involving nickel-based electrodes, enhanced the performance of the electrodes. This procedure led to the formation of NiOOH, exhibiting high electrocatalytic activity. The activation process was carried out CV at a scan rate of  $50 \text{ mV s}^{-1}$  for 200 cycles. A rise in current is caused by the NiOOH production event throughout subsequent cycles. The thickness of the NiOOH layer increases in direct proportion to the number of potential sweeps. The presence of  $\text{OH}^-$  ions can be ascribed to, in accordance with the subsequent equation<sup>55–57</sup>:

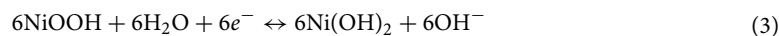
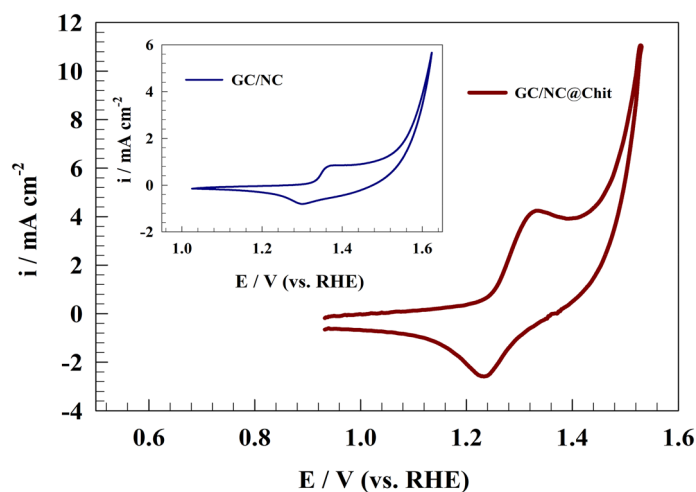
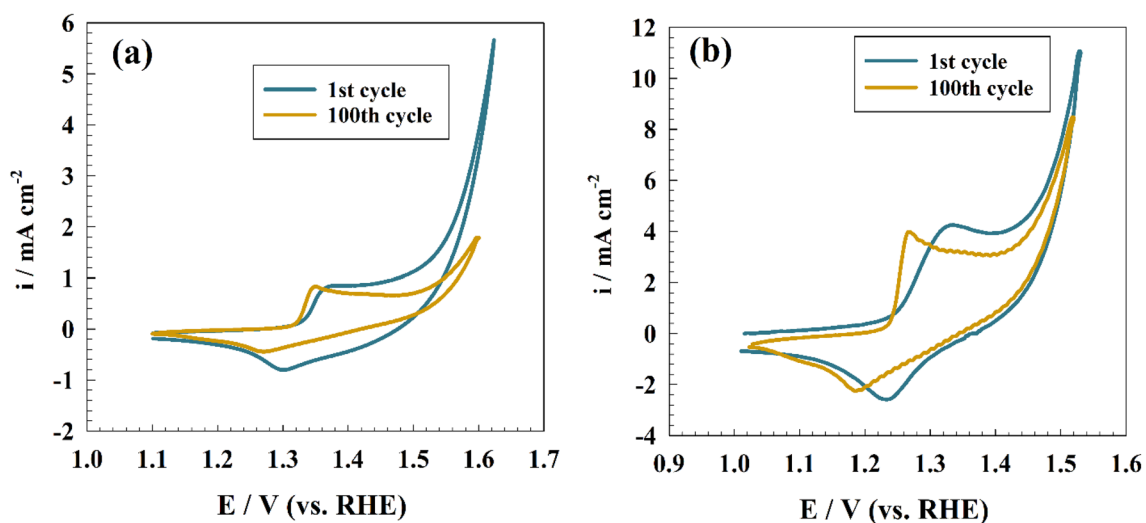


Figure 4 shows the CV of modified GC/NC@Chit electrode in 1.0 M NaOH with corresponding redox peak within the specified potential window (1.2–1.35 V (vs. RHE)) attributed to the conversion of Ni(II) to Ni(III) and vice versa.

Furthermore, the stability of redox species formation for Ni-based electrode was studied using repeated CV of the modified GC/NC and GC/NC@Chit in alkaline medium for 100 cycles. However, the increase in number of CVs in KOH lead to increase the thickness of the  $\text{Ni}(\text{OH})_2/\text{NiOOH}$  layer that responsible for electrode activity. On the other hand, other factors could decrease the electrode current such as surface stability or poisoning. As shown in Fig. 5, the CVs for both GC/NC and GC/NC@Chit before and after 100 cycles in KOH. For GC/NC, the slight shift in peak position due to the increase in thickness owing to conversion of more species to higher



**Figure 4.** CV of modified GC/NC@Chit electrode in a alkaline solution.



**Figure 5.** Stability test for modified (a) GC/NC and (b) GC/NC@Chit electrodes in KOH.

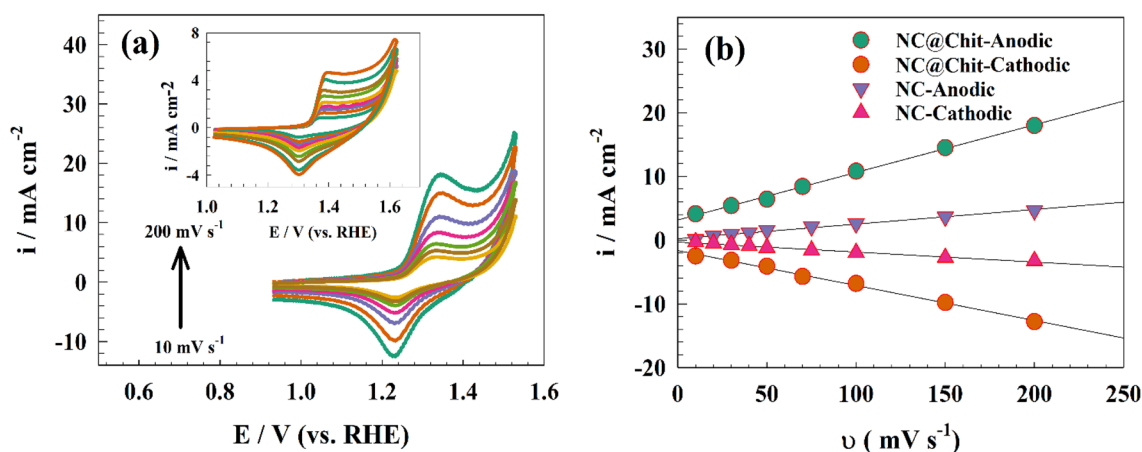


**Figure 6.** (a) CVs of GC/NC@Chit modified electrode at different sweep rates (10–200  $\text{mV s}^{-1}$ ), with inset figure showing CVs of GC/NC electrode at various sweep rates (10–200  $\text{mV s}^{-1}$ ). (b) anodic current vs. scan rate for both GC/NC@Chit and GC/NC electrodes.

electroactive NiOOH that make the process more thermodynamic favored. Else, GC/NC@Chit showed higher current stability along due to the presence of chitosan substrate which enhance the stability of nickel cobaltite on electrode surface.

The CV responses were recorded against different scan rates to confirm the kinetics of the redox process. Figure 6a shows the CV curves of modified GC/NC@Chit electrode at scan rates extending from 10 to 200  $\text{mV s}^{-1}$  with inset figure depicting the linearity of the increasing current response with scan rate. The surface coverage of the NiOOH active species can be calculated using the following equation:

$$i = \left( \frac{n^2 F^2}{4RT} \right) \nu A \Gamma \quad (4)$$

where  $i$  is redox current,  $n = 1$  (number of electrons),  $A = 0.0707 \text{ cm}^2$  (surface area),  $\Gamma$  (surface coverage), and  $\nu$  (scan rate).

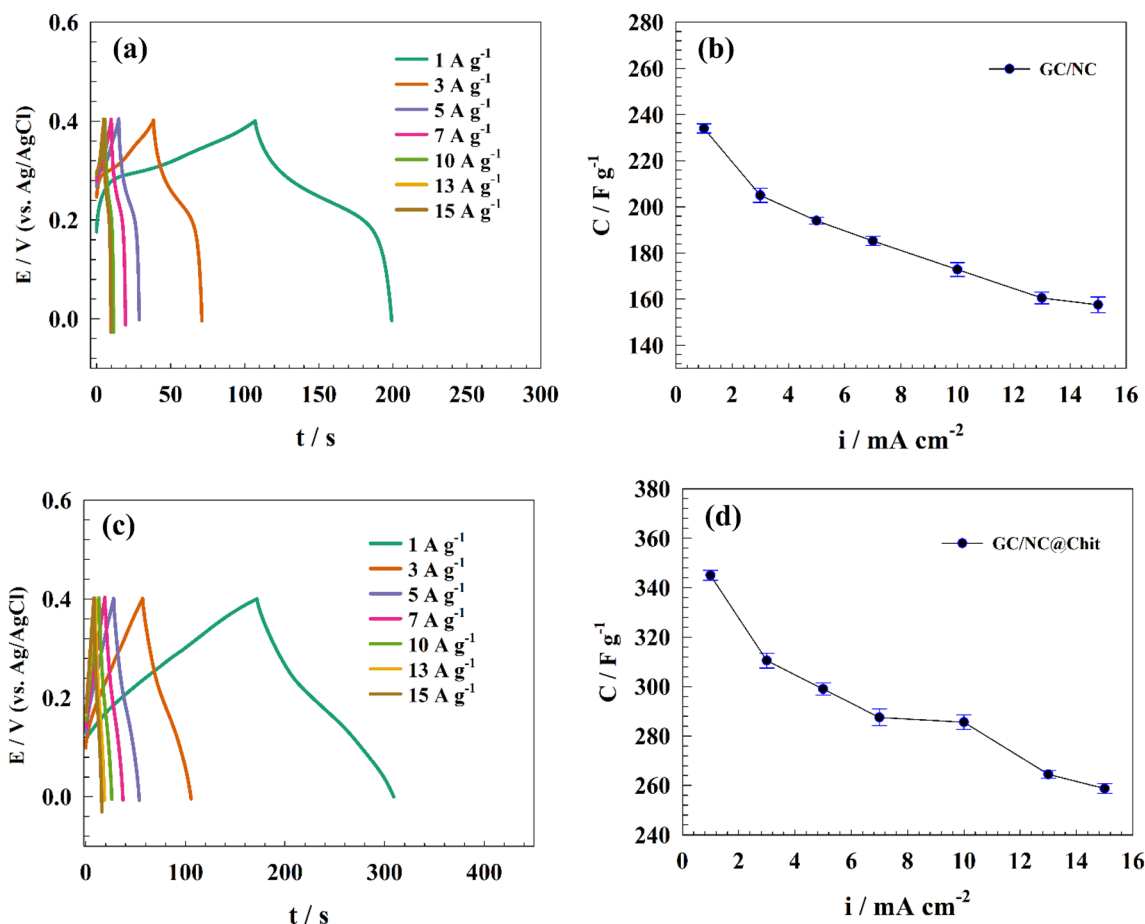
Consequently, surface coverage was estimated from the linear relation between anodic current vs. scan rate (see Fig. 6b). The calculated surface coverage ( $\Gamma$ ) for NC@Chit and /NC are  $1.67 \times 10^{-9}$  and  $8.61 \times 10^{-10} \text{ mol cm}^{-2}$ , respectively.

The NC and NC@Chit composites display uniform distribution across the chitosan sheets, showcasing effective areas and favorable hydrophilic properties. As a result, the GC/NC@Chit composite exhibits a high specific capacitance ( $C_s$ ) value. Figure 7a,c illustrates the GCD curve of the prepared active material, measured at different current densities with pristine nickel cobaltite exhibiting battery-like curve with capacitance (see Fig. 7a). For modified GC/NC electrode, the capacitance value obtained were 234, 205, 194, 185, 173, 160, and 157  $\text{F g}^{-1}$  at different current densities of 1, 3, 7, 10, 13, and 15  $\text{A g}^{-1}$  respectively (see Fig. 7b). On the other hand, spinel oxide incorporation in chitosan sheets exhibited high capacitance of 345, 310, 299, 287, 285, 264, and 258  $\text{F g}^{-1}$  at different current densities of 1, 3, 7, 10, 13, and 15  $\text{A g}^{-1}$  respectively (see Fig. 7d).

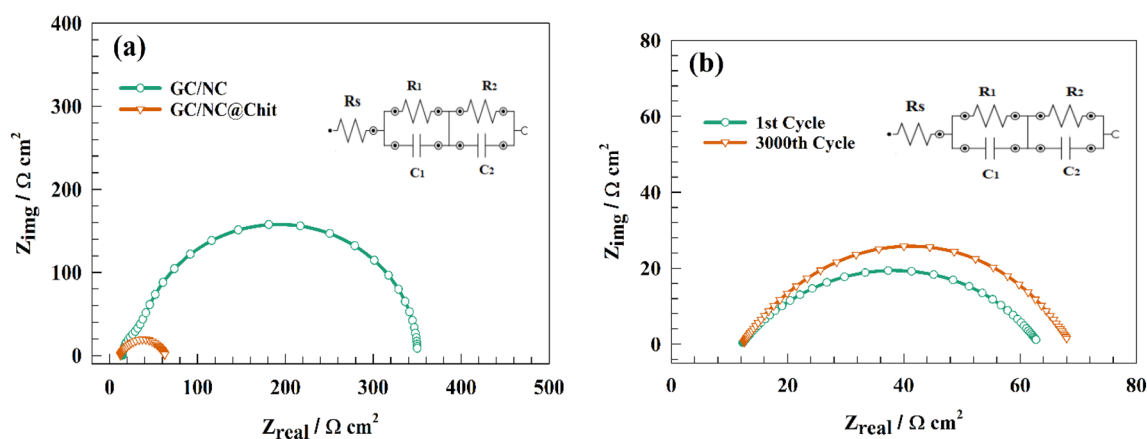
Electrochemical impedance spectroscopy (EIS) measurements were utilized on both the unmodified and modified NC in order to elucidate the performance of the chitosan-based surface compared with the pristine GC/NC electrode. Figure 8a shows the Nyquist plot for NC and NC@Chit electrodes in the alkaline medium in a solution of 1.0 M KOH at a constant potential of 1.4 V (RHE). The presence of a semi-circuit could be attributed to the charge transfer process. Whereas, the lower diameter of the GC/NC@Chit electrode compared to the unmodified NC electrode counterparts represents higher activity of the chitosan-based electrode for Ni(II)/Ni(III) conversion. The equivalent circuit fitting is shown as inset of Fig. 8, where the tabulated values of  $R_s$  (solution resistance) connected to  $R_1$ , and  $R_2$  (charge transfer resistances for outer and inner layer) of the competitive materials are provided in Table 1.

Figure 8b shows EIS of the GC/NC@Chit after stability test. Whereas, shift in solution resistance ( $R_s$ ) was observed after stability test. Otherwise, the charge transfer shifted to higher value because of the decrease of surface electrochemical activity.

The stability test is a crucial parameter for evaluating the performance of supercapacitor materials. However, both NC and NC@Chit composites exhibited remarkable stability characteristics. Figure 9a illustrates the stability of both modified GC NC and GC/NC@Chit electrodes under a current density of 10  $\text{A g}^{-1}$  throughout 3000 cycles. The GC/NC composite exhibited a capacitive retention of 86% after undergoing 3000 cycles, demonstrating a high level of stability. Additionally, GC/NC@Chit electrode demonstrated an impressive capacitive retention of 93% after continuous cycling. The remarkable stability of the GC/NC@Chit composite can be attributed to the robust interaction among nickel cobaltite, chitosan, and the electrode surface, as well as the strong interlayer interaction among the chitosan sheets. Furthermore, based on the data presented in Fig. 9b,c, differences in capacitance and IR drop before and after stability can be observed in the GCD curve.



**Figure 7.** (a) GCD of GC/NC electrode, (b) Relation between capacitance versus applied current for GC/NC electrode, (c) GCD of GC/NC@Chit electrode, (d) Relation between capacitance versus applied current for GC/NC@Chit electrode.



**Figure 8.** (a) Representation of EIS plot of NC and NC@Chit surfaces at constant potential equal 1.4 V. (b) Nyquist plot of the modified GC/NC@Chit after 3000th GCD cycles.

Electrode	R <sub>s</sub> (Ω cm <sup>2</sup> )	R <sub>1</sub> (Ω cm <sup>2</sup> )	C <sub>1</sub> (F)	R <sub>2</sub> (Ω cm <sup>2</sup> )	C <sub>2</sub> (F)
GC/NC	14.8	24.9	0.00068616	360.2	0.00013797
GC/NC@Chit	12.1	21.8	0.00142678	71.3	0.0012675

**Table 1.** EIS fitting parameters for Nyquist plot of different modified surfaces.

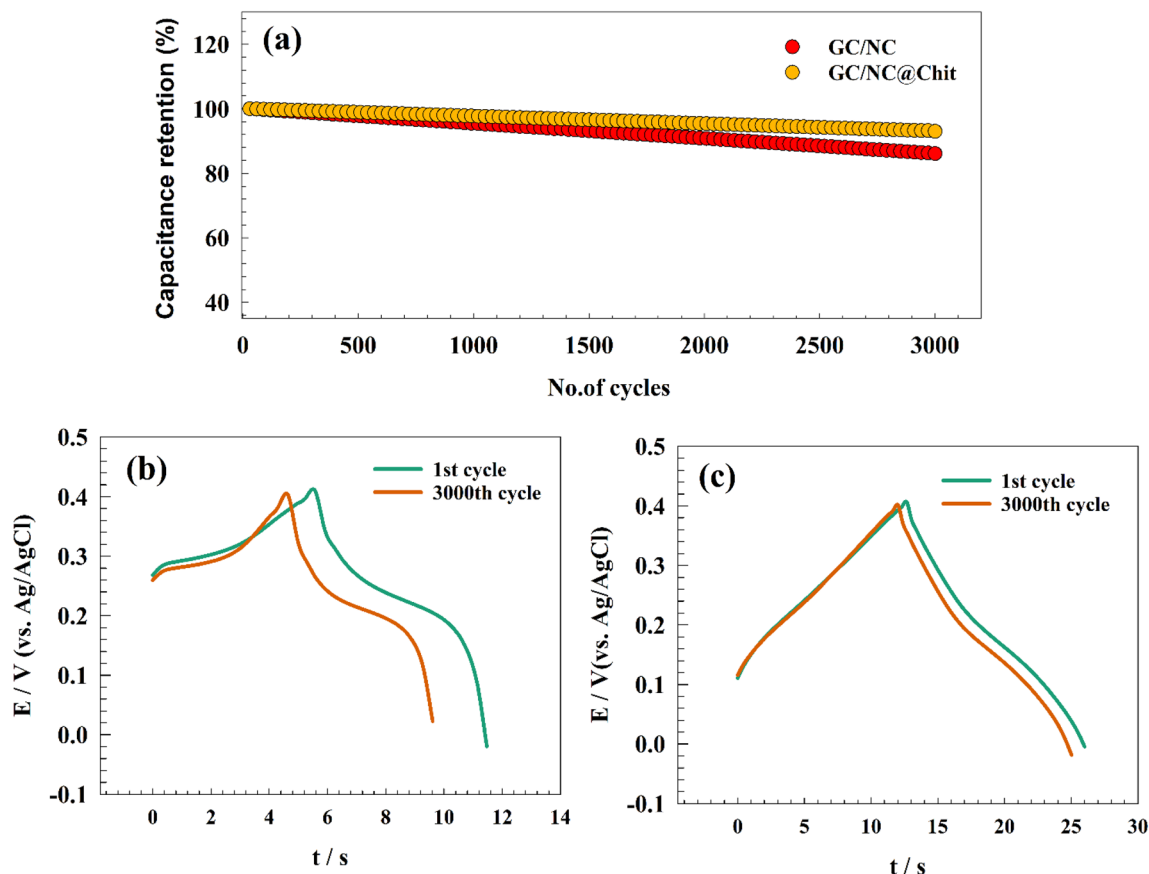


**Figure 9.** (a) Repeated GCD of modified GC/NC, and GC/NC@Chit, Comparison between 1st versus 3000th cycles for (b) GC/NC, and (c) GC/NC@Chit.

### Water splitting application

The oxygen evolution process holds significant importance in the functioning of fuel cells and batteries, as it facilitates the conversion of chemical energy to electrical energy<sup>58,59</sup>. Various electrochemical methods have been utilized to determine the mechanism of the oxygen evolution reaction.

One of the prevalent pathways for the electrochemical conversion of hydroxide to molecular oxygen involves a two-step electrochemical process.

The initial step involved the adsorption of hydroxide ions onto the electrode surface, resulting in the formation of hydroxide adsorbates. Subsequently, the adsorbed hydroxide species interacted with hydroxide ions present in the surrounding medium, producing adsorbed oxygen species. The ultimate stage involves the discharge of adsorbed atomic oxygen, resulting in the production of molecular oxygen.

The operational framework of oxygen evolution reactions (OER) can be established in the following manner<sup>60</sup>:

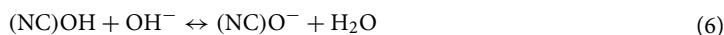
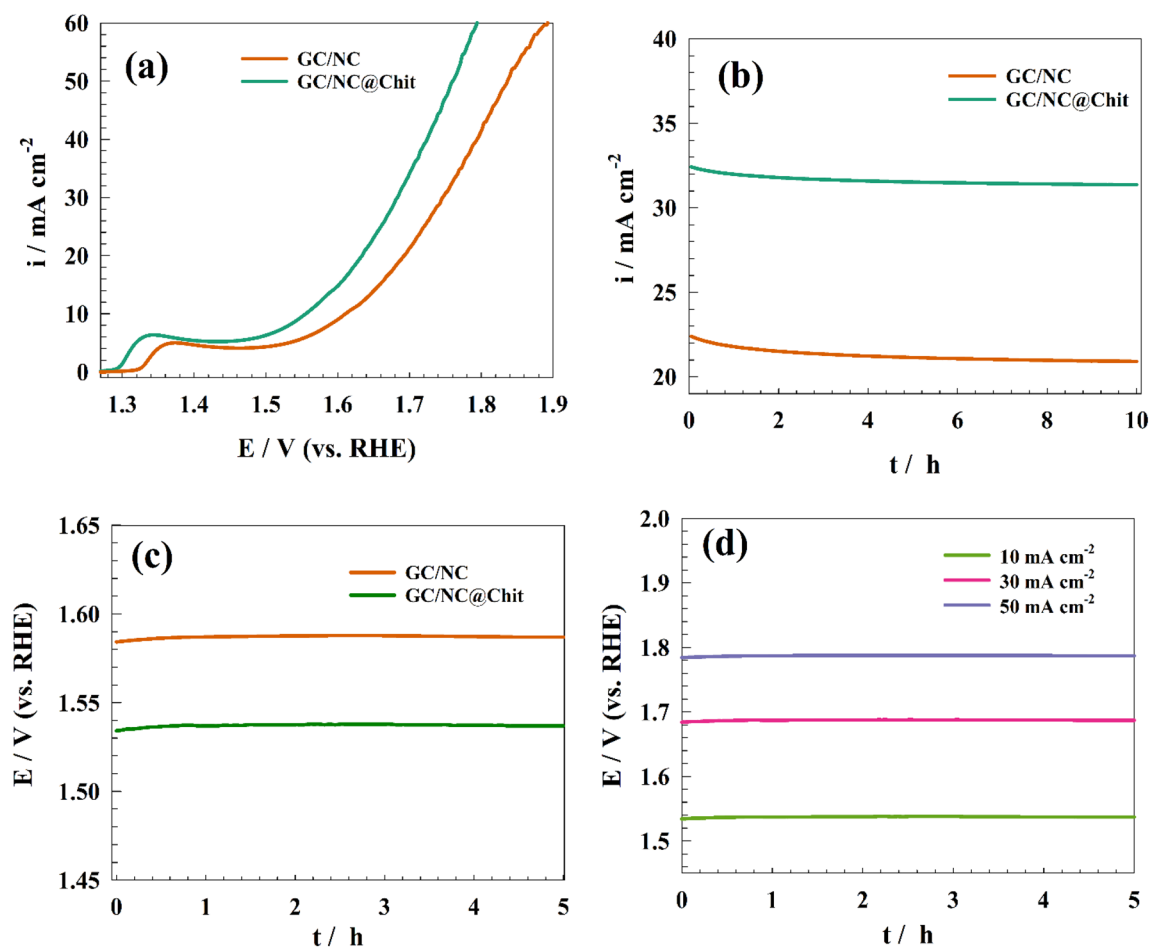


Figure 10a depicts the OER (oxygen evolution reaction) on the GC/NC and GC/NC@Chit under the influence of 1.0 M NaOH. As per the analysis, a single oxidation peak can be attributed to converting Ni(II) to Ni(III) where the GC/NC@Chit exhibited a notable current density for oxygen evolution reaction (OER) at a comparatively reduced potential than its GC/NC equivalent.

Furthermore, the electrode's durability in the OER holds significance in electrochemical splitting of water. Chronoamperometry was used to examine the sustained durability of the electrode concerning the (OER). Figure 10b illustrates the chronoamperogram of the GC/NC and GC/NC@Chit modified electrodes in a 1.0 M NaOH solution, with a consistent potential of 1.7 V (versus RHE). The current density of GC/NC and GC/NC@Chit demonstrated a corresponding reduction in its initial value by 8.4 and 4.7%. The current reduction presently observed is attributed to the mechanical corrosion of the electrocatalyst's surface caused by the evolved gases





**Figure 10.** (a) LSV of the NC and NC@Chit for OER, (b) Chronoamperogram for OER over different surfaces, (c) Chronopotentiogram of different modified surfaces for OER, (d) Chronopotentiogram of modified GC/NC@Chit at different constant current densities.

passing through. Additionally, the electrodes' enhanced long-term durability towards OER is demonstrated by the slight fluctuations in the oxidation current.

In addition, the electrode's galvanostatic endurance was examined for OER. The constant potential chronopotentiometry for two modified surfaces, GC/NC and GC/NC@Chit, is shown in Fig. 10c at a current of  $10 \text{ mA cm}^{-2}$ . As seen, the electrode's overpotential ( $\eta$ ) reached 440 and 310 mV, respectively which could be ascribed to superior OER capability of the chitosan-based electrode. Additionally, modified GC/NC@Chit was tested for galvanostatic stability at varied current densities, including 10, 30, and  $50 \text{ mA cm}^{-2}$ , in a solution of 1.0 M NaOH. While at an overpotential of 310, 470, and 630 mV for a current density of 10, 30, and  $50 \text{ mA cm}^{-2}$  (see Fig. 10d). A comparative evaluation of the NC@Chit electrode's performance for oxygen evolution reaction (OER) in relation to other composites is provided in Table 2.

Surface	$\eta$ (mV)@ $10 \text{ mA cm}^{-2}$	Tafel slope ( $\text{mV dec}^{-1}$ )	Electrolyte	References
GC/NC@Chit	310	67	1.0 M NaOH	This work
NiCo nanosheets	332	41	1.0 M KOH	61
1D- $\text{NiCo}_2\text{O}_4$	260	104	1.0 M KOH	62
GC/ $\text{Co}_3\text{O}_4$	270	64	1.0 M KOH	63
GC/ $\text{LiCoO}_2$	430	48	1.0 M KOH	64
GC/NiCo-LDH	335	41	1.0 M KOH	65
GC/ $\text{NiFe}_2\text{O}_4$	440	98	0.1 M KOH	66
$\text{PdO@CoNi}_2\text{S}_4$	230	72	1.0 M KOH	67
$\text{PdONPs@Co}_3\text{O}_4$	250	58	0.1 M KOH	68

**Table 2.** Comparative evaluation GC/NC@Chit electrode and other modified electrodes mentioned in the literature for OER.

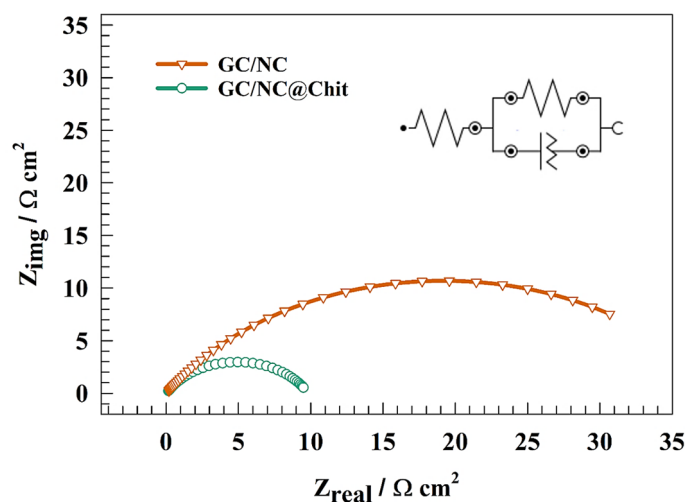


**Figure 11.** Representation of EIS plot of NC and NC@Chit surfaces at constant potential for OER.

Electrode	$R_s$ ( $\Omega \text{ cm}^2$ )	$R_{ct}$ ( $\Omega \text{ cm}^2$ )	Q	
			Y0 (F)	n
GC/NC	1.24	37	0.0001894	0.647
GC/NC@Chit	0.98	11	0.0003871	0.547

**Table 3.** EIS fitting parameters for Nyquist plot of different modified surfaces for OER.

The charge transfer resistance across different electrode surfaces was determined using electrochemical impedance spectroscopy. The Nyquist plot representation of various electrodes, GC/NC and GC/NC@Chit was obtained in 1.0 M NaOH. The experiment was carried at a constant potential of 1.6 V (versus RHE), as shown in Fig. 11.

The fitting circuit that corresponds to the charge-transfer is shown in the inset of Fig. 11. To address the non-uniformity of the electrode surfaces, a constant phase element (CPE) is utilized in place of the capacitive component. The resistances  $R_s$ ,  $R_c$ , and  $Q_1$  are commonly referred to as the solution resistance, charge transfer resistance, and constant phase element for layers. The computed fitting parameters are presented in Table 3. The charge transfer resistance of the GC/NC was measured to be  $37 \Omega \text{ cm}^2$ , whereas the GC/NC@Chit surfaces exhibited a lower resistance of  $13 \Omega \text{ cm}^2$ . The increased efficiency of oxygen evolution observed in GC/NC@Chit, as compared to pure GC/NC, can be attributed to the decrease of resistance's values.

The study investigated HER on surfaces modified with NC and NC@Chit. Figure 12a shows the modified electrode's linear sweep voltammetry in a solution of 1.0 M NaOH.

The superior electrocatalytic performance of the modified GC/NC@Chit compared to the unmodified GC/NC can be attributed to the incorporation of chitosan into the electrocatalyst frameworks, enhancing both electronic and adsorption properties. The mechanism for HER in a medium with high alkalinity involves a reversible reaction between two molecules of water and two electrons, forming two adsorbed hydrogen atoms and two hydroxide ions. The Volmer step pertains to the dissociation of water. The corresponding Tafel step involves the reversible reaction between two hydrogen atoms adsorbed on a surface and forming a hydrogen molecule. However, the modified electrode had efficient HER at onset potential of  $-0.26$ ,  $-0.2$  V for NC and /NC@Chit surfaces, respectively. The current density reached  $50 \text{ mA cm}^{-2}$  at overpotential of  $-0.48$  and  $-0.37$  V for NC and NC@Chit surfaces, respectively.

Figure 12b illustrates the chronoamperogram of the GC/NC and GC/NC@Chit modified electrodes in a solution 1.0 M NaOH, with a consistent potential of  $-0.3$  V (versus the reversible hydrogen electrode, RHE). The measured current density exhibited a reduction of 14.3% and 12.6% for the GC/NC and GC/NC@Chit, respectively. The current decrease currently being observed is ascribed to the mechanical degradation of the electrocatalyst surface caused by the release of gases through said surface. The performance of our modified electrode in terms of hydrogen production was evaluated with other catalyst and is tabulated in Table 4.

However, slight deviations in the reduction current demonstrate the improved long-term durability of the electrodes in relation to the HER. Additionally, an investigation was conducted to assess the galvanostatic durability of the electrode for the HER. Figure 12c illustrates the application of constant potential chronopotentiometry at a consistent current density of  $10 \text{ mA cm}^{-2}$  across various modified surfaces, specifically GC/NC and GC/NC@Chit. Consequently, the electrode attained the potentials of  $-0.33$  and  $-0.22$  V, respectively. The decreased overpotential observed in the chitosan-based electrode can be attributed to its enhanced efficiency in facilitating the hydrogen evolution process. In addition, galvanostatic stability testing was conducted on modified GC/NC@

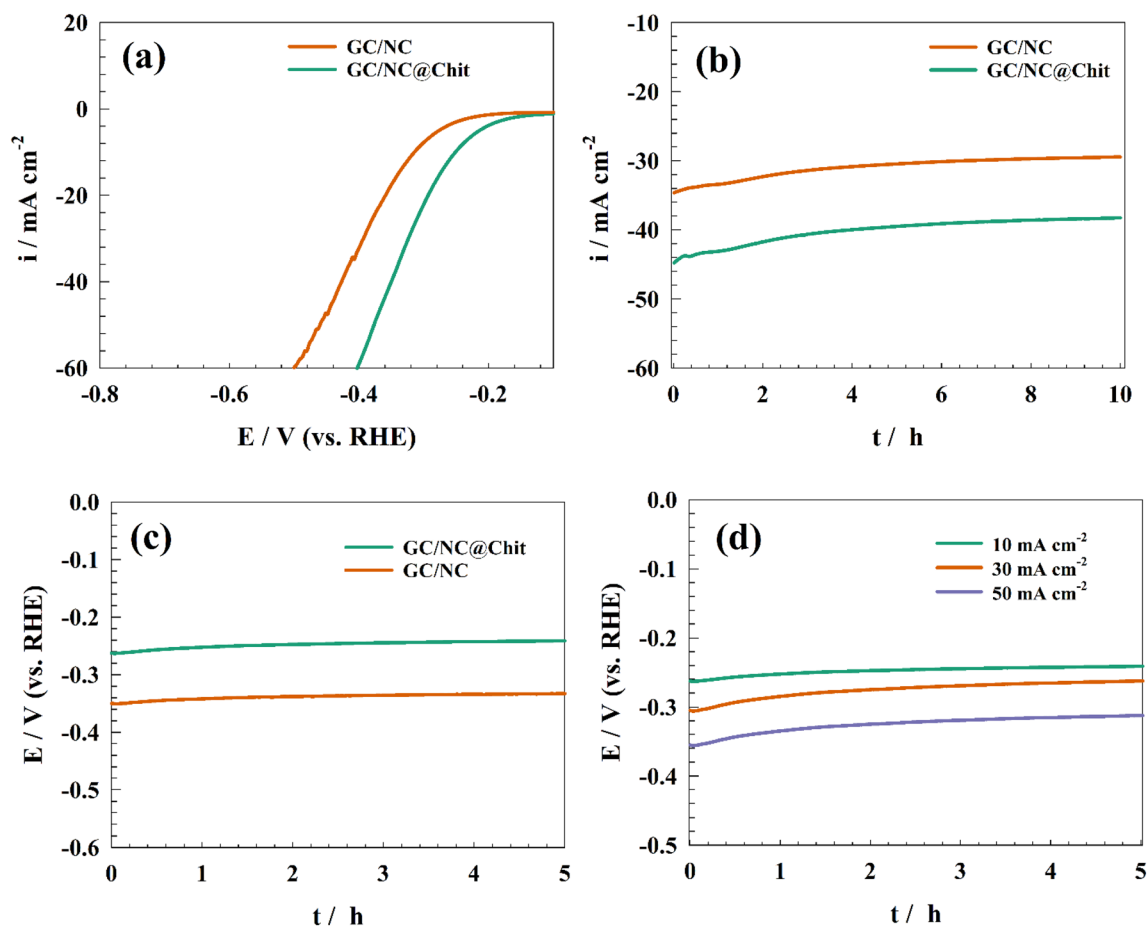


**Figure 12.** (a) Representation of LSV of the NC and NC@Chit for HER, (b) Chronopotentiogram of different modified surfaces for HER, (c) Chronopotentiogram of different modified surfaces for HER, (d) Chronopotentiogram of modified GC/NC@Chit at different constant current densities.

Surface	$\eta$ (mV)@10 $\text{mA cm}^{-2}$	Tafel slope ( $\text{mV dec}^{-1}$ )	Electrolyte	References
GC/NC@Chit	-240	71	1.0 M NaOH	This work
$\text{Co}_2\text{FeO}_4/\text{rGO}$	-260	48	1.0 M KOH	69
$\text{Ni}_2\text{Fe/N}$ -doped porous C	-198	83	1.0 M KOH	70
Ni/NiO core/shell nanosheets	-145	43	1.0 M KOH	71
GC/Ag@CNT	-570	148	0.5 M NaOH	48
NiFe-LDH/MXene/Ni foam	-132	70	1.0 M KOH	72

**Table 4.** Comparative evaluation GC/NC@Chit electrode and other modified electrodes for HER.

Chit in a 1.0 M NaOH solution at various current densities, including 10, 30, and 50  $\text{mA cm}^{-2}$ . In contrast, the electrode achieved a current density of 50  $\text{mA cm}^{-2}$  when the overpotential was measured at -360 mV. (Refer to Fig. 12d).

EIS was used to confirm the charge transfer resistance across diverse electrode surfaces. As illustrated in Fig. 13, Nyquist representation for different surfaces of NC and NC@Chit, was acquired in a solution with a concentration of 1.0 M NaOH. The potential was kept constant at -0.3 V (vs. RHE).

The corresponding fitting equivalent circuit is displayed in the inset of Fig. 13 with use of a constant phase element (CPE) as a replacement for the capacitive element in order to mitigate the non-homogeneity of the electrode surfaces. Table 5 displays the calculated fitting elements. The GC/NC@Chit material demonstrated a charge transfer resistance of 134  $\Omega \text{ cm}^2$ , whereas the GC/NC@Chit surfaces exhibited a resistance of 58  $\Omega \text{ cm}^2$ . The superior performance of GC/NC@Chit in hydrogen evolution as compared to pure GC/NC can be ascribed to the reduced charge transfer resistance.

Furthermore, Tafel slopes are essential parameters in kinetic studies. In Fig. 14a, the Tafel slopes for OER and HER of modified GC/NC and GC/NC@Chit are depicted with values of 79 and 67  $\text{mV dec}^{-1}$ , respectively. The lower value for chitosan modified electrode indicated that the OER was favored over GC/NC@Chit compared

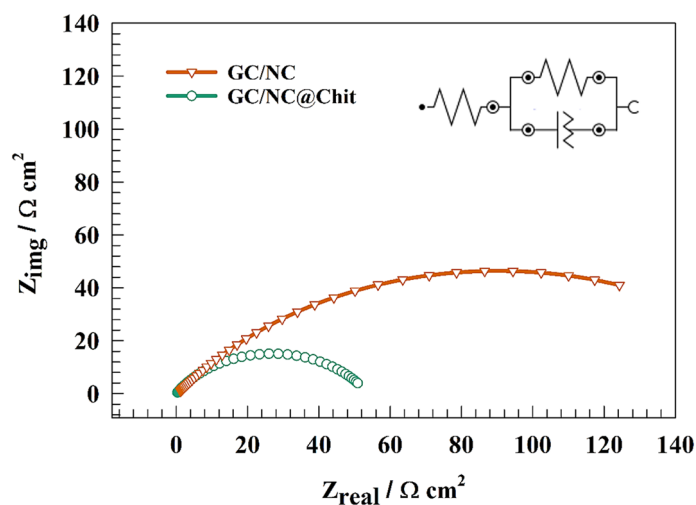


**Figure 13.** Representation of EIS plot of NC and NC@Chit surfaces at constant potential for HER.

Electrode	$R_s$ ( $\Omega \text{ cm}^2$ )	$R_{ct}$ ( $\Omega \text{ cm}^2$ )	Q	
			$Y_0$ (F)	n
GC/NC	3.4	134	0.0000786	0.513
GC/NC@Chit	4.45	58	0.0001224	0.568

**Table 5.** EIS fitting parameters for Nyquist plot of different modified surfaces for HER.

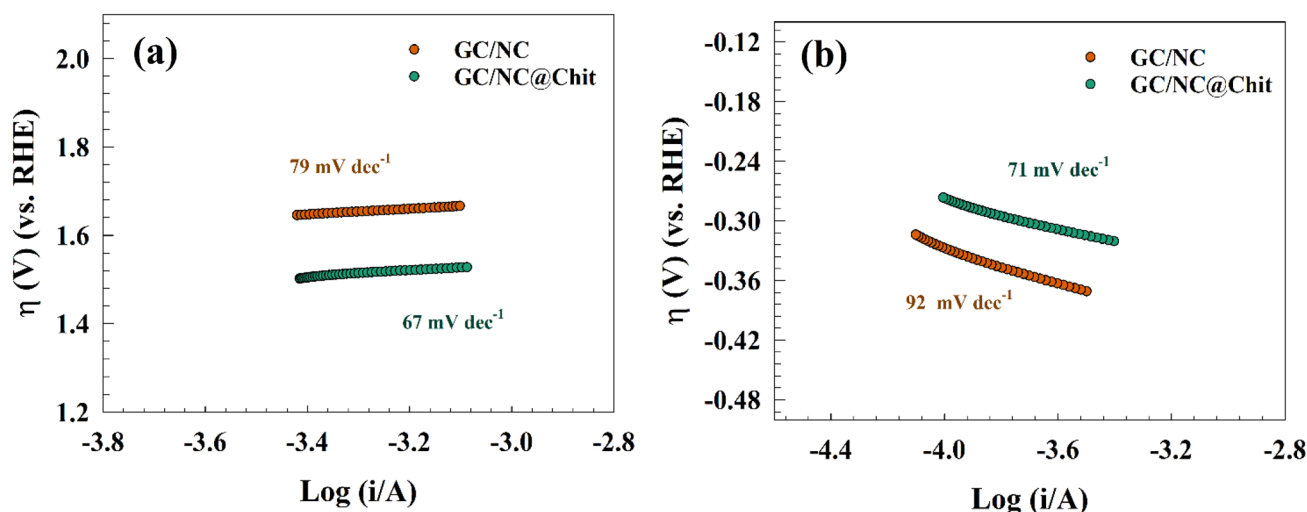


**Figure 14.** Tafel plot of NC and NC@Chit surfaces for (a) OER and (b) HER.

with pristine GC/NC counterparts. The values of Tafel slopes were comparable with others reported in the literature for surfaces such as  $136 \text{ mV dec}^{-1}$  for NiO/C composite<sup>73</sup> and  $110 \text{ mV dec}^{-1}$  for  $\text{Fe}(\text{TCNQ})_2/\text{Fe}$ <sup>74</sup>. Furthermore, Tafel provided slopes for HER are  $92$  and  $71 \text{ mV dec}^{-1}$  for GC/NC and GC/NC@Chit, respectively (see Fig. 14b). The values of Tafel slopes matched with those reported in literature like  $135 \text{ mV dec}^{-1}$  for Ni/NiO nanosheets<sup>75</sup>,  $132 \text{ mV dec}^{-1}$  for Co-S/CF<sup>76</sup>, and  $148 \text{ mV dec}^{-1}$  for Ag@CNT<sup>48</sup>.

## Conclusion

In conclusion, the synthesis of a composite material incorporating chitosan proved to be a successful strategy for enhancing the efficiency of both oxygen and hydrogen evolution. Comparative studies between pristine and chitosan-based NC revealed a synergistic effect, with the electrodes modified with GC/NC@Chit demonstrating notable efficacy in both capacitors and water-splitting applications. The pristine nickel cobaltite exhibited battery-like behavior, while the chitosan-based nickel cobaltite showed capacitor-like activity. Both modified

electrodes showed high capacitance in an alkaline medium with provided values of 234 and 345 F g<sup>-1</sup> (@1Ag<sup>-1</sup>). Additionally, high structure stability of spinel oxides characterized by repeated GCD represented high capacitance retention equaled 86, and 93% for NC and NC@Chit, respectively. The recorded current values were 50 mA cm<sup>-2</sup> at 1.88 and -0.36 V (vs. RHE) for OER and HER, respectively. The Tafel slope value ensured the water splitting favorability, whereas the lower value reflects the easier electron transfer process. Thus, the provided Tafel slopes at GC/NC@Chit are 67 and 71 mV dec<sup>-1</sup> for OER and HER, respectively. Finally, the long-term stability reflected the good durability of GC/NC@Chit towards water splitting application.

## Data availability

The datasets used and/or analyzed during the current study are available from the corresponding author on reasonable request.

Received: 11 August 2023; Accepted: 11 December 2023

Published online: 30 January 2024

## References

1. Maila, M. P. & Cloete, T. E. The use of biological activities to monitor the removal of fuel contaminants—perspective for monitoring hydrocarbon contamination: A review. *Int. Biodeterior. Biodegradation* **55**, 1–8 (2005).
2. Li, X., Wang, X., Weng, L., Zhou, Q. & Li, Y. Microbial fuel cells for organic-contaminated soil remedial applications: A review. *Energy Technol.* **5**, 1156–1164 (2017).
3. Conte, M., Iacobazzi, A., Ronchetti, M. & Vellone, R. Hydrogen economy for a sustainable development: State-of-the-art and technological perspectives. *J. Power Sources* **100**, 171–187 (2001).
4. Arsal, A. Z. *et al.* Hydrogen energy storage integrated hybrid renewable energy systems: A review analysis for future research directions. *Int. J. Hydrog. Energy* **47**, 17285–17312 (2022).
5. Midilli, A., Ay, M., Dincer, I. & Rosen, M. A. On hydrogen and hydrogen energy strategies: I: Current status and needs. *Renew. Sustain. Energy Rev.* **9**, 255–271 (2005).
6. Dincer, I. & Acar, C. A review on clean energy solutions for better sustainability. *Int. J. Energy Res.* **39**, 585–606 (2015).
7. Ahmed, S. F. *et al.* Sustainable hydrogen production: Technological advancements and economic analysis. *Int. J. Hydrog. Energy* **47**, 37227–37255 (2022).
8. Sharma, S., Agarwal, S. & Jain, A. Significance of hydrogen as economic and environmentally friendly fuel. *Energies* **14**, 7389 (2021).
9. Abad, A. V. & Dodds, P. E. Green hydrogen characterisation initiatives: Definitions, standards, guarantees of origin, and challenges. *Energy Policy* **138**, 111300 (2020).
10. Hefnawy, M. A., Fadlallah, S. A., El-Sherif, R. M. & Medany, S. S. Competition between enzymatic and non-enzymatic electrochemical determination of cholesterol. *J. Electroanal. Chem.* **930**, 117169. <https://doi.org/10.1016/j.jelechem.2023.117169> (2023).
11. Kumar, S. *et al.* Electronic and structural disorder of NiCo<sub>2</sub>O<sub>4</sub> nanostructures using phytochemicals from desert gourd offered efficient asymmetric supercapacitor and oxygen evolution reaction. *J. Energy Storage* **72**, 108728. <https://doi.org/10.1016/j.est.2023.108728> (2023).
12. Abbas, Z. *et al.* Exploring the electrochemical utilization of PANI/CNT-integrated Ni–Mn phosphates for advanced supercapacitor applications. *Electrochim. Acta* **471**, 143350. <https://doi.org/10.1016/j.electacta.2023.143350> (2023).
13. Gamal, H., Elshahawy, A. M., Medany, S. S., Hefnawy, M. A. & Shalaby, M. S. Recent advances of vanadium oxides and their derivatives in supercapacitor applications: A comprehensive review. *J. Energy Storage* **76**, 109788. <https://doi.org/10.1016/j.est.2023.109788> (2024).
14. Fawzy, S. M., Khedr, G. E. & Allam, N. K. Electronically defective tellurium-doped TiO<sub>2</sub> catalysts for enhanced photoelectrochemical water splitting. *Int. J. Hydrog. Energy* **48**, 33111–33118. <https://doi.org/10.1016/j.ijhydene.2023.05.037> (2023).
15. Sultan, S. *et al.* Single atoms and clusters based nanomaterials for hydrogen evolution, oxygen evolution reactions, and full water splitting. *Adv. Energy Mater.* **9**, 1900624 (2019).
16. Sarkar, S. & Peter, S. C. An overview on Pd-based electrocatalysts for the hydrogen evolution reaction. *Inorg. Chem. Front.* **5**, 2060–2080 (2018).
17. Shan, A. *et al.* Interfacial electronic structure modulation of Pt–MoS<sub>2</sub> heterostructure for enhancing electrocatalytic hydrogen evolution reaction. *Nano Energy* **94**, 106913 (2022).
18. Chen, S., Duan, J., Jaroniec, M. & Qiao, S. Z. Three-dimensional N-doped graphene hydrogel/NiCo double hydroxide electrocatalysts for highly efficient oxygen evolution. *Angew. Chemie Int. Ed.* **52**, 13567–13570. <https://doi.org/10.1002/anie.201306166> (2013).
19. Cai, J. *et al.* Fabrication of three-dimensional nanoporous nickel films with tunable nanoporosity and their excellent electrocatalytic activities for hydrogen evolution reaction. *Int. J. Hydrog. Energy* **38**, 934–941. <https://doi.org/10.1016/j.ijhydene.2012.10.084> (2013).
20. Chen, W. *et al.* Hydrogen-evolution catalysts based on non-noble metal nickel–molybdenum nitride nanosheets. *Angew. Chemie Int. Ed.* **51**, 6131–6135 (2012).
21. Drosou, M., Kamatsos, F. & Mitsopoulou, C. A. Recent advances in the mechanisms of the hydrogen evolution reaction by non-innocent sulfur-coordinating metal complexes. *Inorg. Chem. Front.* **7**, 37–71 (2020).
22. Medany, S. S. & Hefnawy, M. A. Nickel–cobalt oxide decorated Chitosan electrocatalyst for ethylene glycol oxidation. *Surf. Interfaces* **40**, 103077. <https://doi.org/10.1016/j.surfint.2023.103077> (2023).
23. Tian, J. *et al.* Self-supported NiMo hollow nanorod array: an efficient 3D bifunctional catalytic electrode for overall water splitting. *J. Mater. Chem. A* **3**, 20056–20059 (2015).
24. Bodhankar, P. M., Sarawade, P. B., Singh, G., Vinu, A. & Dhawale, D. S. Recent advances in highly active nanostructured NiFe LDH catalyst for electrochemical water splitting. *J. Mater. Chem. A* **9**, 3180–3208 (2021).
25. Bashal, A. H. *et al.* Green synthesis of NiFe<sub>2</sub>O<sub>4</sub> nano-spinel oxide-decorated carbon nanotubes for efficient capacitive performance—Effect of electrolyte concentration. *Nanomaterials* **13**, 2643. <https://doi.org/10.3390/nano13192643> (2023).
26. Hefnawy, M. A., Medany, S. S., El-Sherif, R. M. & Fadlallah, S. A. Green synthesis of NiO/Fe<sub>2</sub>O<sub>3</sub>@chitosan composite catalyst based on graphite for urea electro-oxidation. *Mater. Chem. Phys.* **290**, 126603. <https://doi.org/10.1016/j.matchemphys.2022.126603> (2022).
27. Hefnawy, M. A., Fadlallah, S. A., El-Sherif, R. M. & Medany, S. S. Nickel–manganese double hydroxide mixed with reduced graphene oxide electrocatalyst for efficient ethylene glycol electrooxidation and hydrogen evolution reaction. *Synth. Met.* **282**, 116959. <https://doi.org/10.1016/j.synthmet.2021.116959> (2021).
28. Hasan, M. M. *et al.* Highly durable compositionally variant bifunctional tetrametallic Ni–Co–Mn–Fe phosphide electrocatalysts synthesized by a facile electrodeposition method for high-performance overall water splitting. *Energy Fuels* **36**, 14371–14381. <https://doi.org/10.1021/acs.energyfuels.2c03266> (2022).

29. Vikraman, D. *et al.* Spinel-structured metal oxide-embedded MXene nanocomposites for efficient water splitting reactions. *Inorg. Chem. Front.* **9**, 5903–5916. <https://doi.org/10.1039/D2QI01564A> (2022).
30. Berglund, S. P. *et al.* Comprehensive evaluation of CuBi<sub>2</sub>O<sub>4</sub> as a photocathode material for photoelectrochemical water splitting. *Chem. Mater.* **28**, 4231–4242 (2016).
31. Hussain, S. *et al.* Fabrication of CuFe<sub>2</sub>O<sub>4</sub>/α-Fe<sub>2</sub>O<sub>3</sub> composite thin films on FTO coated glass and 3-D nanospike structures for efficient photoelectrochemical water splitting. *ACS Appl. Mater. Interfaces* **8**, 35315–35322 (2016).
32. Zhu, X. *et al.* Spinel structural disorder influences solar-water-splitting performance of ZnFe<sub>2</sub>O<sub>4</sub> nanorod photoanodes. *Adv. Mater.* **30**, 1801612 (2018).
33. Wang, D. *et al.* Bulk and surface dual modification of nickel–cobalt spinel with ruthenium toward highly efficient overall water splitting. *Appl. Catal. B Environ.* **305**, 121081 (2022).
34. Alamro, F. S. *et al.* Chitosan supports boosting NiCo<sub>2</sub>O<sub>4</sub> for catalyzed urea electrochemical removal application. *Polymers (Basel)* **15**, 3058. <https://doi.org/10.3390/polym15143058> (2023).
35. Simon, P. & Gogotsi, Y. Materials for electrochemical capacitors. *Nat. Mater.* **7**, 845–854 (2008).
36. El Sharkawy, H. M., Elbanna, A. M., Khedr, G. E. & Allam, N. K. Compositionally variant bimetallic Cu–Mn oxysulfide electrodes with meritorious supercapacitive performance and high energy density. *Energy Adv.* <https://doi.org/10.1039/D3YA00415E> (2023).
37. Huang, J., Sumpter, B. G. & Meunier, V. Theoretical model for nanoporous carbon supercapacitors. *Angew. Chemie* **120**, 530–534 (2008).
38. Chen, P.-C., Shen, G., Shi, Y., Chen, H. & Zhou, C. Preparation and characterization of flexible asymmetric supercapacitors based on transition-metal-oxide nanowire/single-walled carbon nanotube hybrid thin-film electrodes. *ACS Nano* **4**, 4403–4411 (2010).
39. Bao, L. & Li, X. Towards textile energy storage from cotton T-shirts. *Adv. Mater.* **24**, 3246–3252. <https://doi.org/10.1002/adma.201200246> (2012).
40. Yan, J. *et al.* Advanced asymmetric supercapacitors based on Ni(OH)<sub>2</sub>/graphene and porous graphene electrodes with high energy density. *Adv. Funct. Mater.* **22**, 2632–2641. <https://doi.org/10.1002/adfm.201102839> (2012).
41. Yuan, C. *et al.* Growth of ultrathin mesoporous Co<sub>3</sub>O<sub>4</sub> nanosheet arrays on Ni foam for high-performance electrochemical capacitors. *Energy Environ. Sci.* **5**, 7883–7887. <https://doi.org/10.1039/C2EE21745G> (2012).
42. Jiang, J. *et al.* Recent advances in metal oxide-based electrode architecture design for electrochemical energy storage. *Adv. Mater.* **24**, 5166–5180. <https://doi.org/10.1002/adma.201202146> (2012).
43. Lang, X., Hirata, A., Fujita, T. & Chen, M. Nanoporous metal/oxide hybrid electrodes for electrochemical supercapacitors. *Nat. Nanotechnol.* **6**, 232–236 (2011).
44. Yang, L. *et al.* Hierarchical network architectures of carbon fiber paper supported cobalt oxide nanonet for high-capacity pseudocapacitors. *Nano Lett.* **12**, 321–325. <https://doi.org/10.1021/nl203600x> (2012).
45. Dubal, D. P., Gomez-Romero, P., Sankapal, B. R. & Holze, R. Nickel cobaltite as an emerging material for supercapacitors: An overview. *Nano Energy* **11**, 377–399. <https://doi.org/10.1016/j.nanoen.2014.11.013> (2015).
46. Xu, C. *et al.* Graphene-based electrodes for electrochemical energy storage. *Energy Environ. Sci.* **6**, 1388–1414. <https://doi.org/10.1039/C3EE23870A> (2013).
47. Wang, H., Gao, Q. & Jiang, L. Facile approach to prepare nickel cobaltite nanowire materials for supercapacitors. *Small* **7**, 2454–2459. <https://doi.org/10.1002/smll.201100534> (2011).
48. Hefnawy, M. A., Nafady, A., Mohamed, S. K. & Medany, S. S. Facile green synthesis of Ag/carbon nanotubes composite for efficient water splitting applications. *Synth. Met.* **294**, 117310. <https://doi.org/10.1016/j.synthmet.2023.117310> (2023).
49. Yu, X.-Y. *et al.* Facile synthesis of urchin-like NiCo<sub>2</sub>O<sub>4</sub> hollow microspheres with enhanced electrochemical properties in energy and environmentally related applications. *ACS Appl. Mater. Interfaces* **6**, 3689–3695. <https://doi.org/10.1021/am4060707> (2014).
50. Muflikhah, M., Rusdianto, B., Putra, E. & Nuryono, N. Modification of silica coated on iron sand magnetic material with chitosan for adsorption of Au(III). *Indones. J. Chem.* **17**, 264. <https://doi.org/10.22146/ijc.22549> (2017).
51. Semwal, A., Singh, B., Archana, D., Verma, A. & Dutta, P. Macromolecular chitosan/ciprofloxacin pro-drugs: synthesis, physico-chemical and biological assessment for drug delivery systems. *J. Polym. Mater.* **29**, 1–13 (2012).
52. Tiwari, S. *et al.* Oxygen and cerium defects mediated changes in structural, optical and photoluminescence properties of Ni substituted CeO<sub>2</sub>. *J. Alloys Compd.* **782**, 689–698 (2019).
53. Ikram, M. *et al.* Novel Ta/chitosan-doped CuO nanorods for catalytic purification of industrial wastewater and antimicrobial applications. *RSC Adv.* **12**, 16991–17004 (2022).
54. Vijayaprasath, G. *et al.* Role of nickel doping on structural, optical, magnetic properties and antibacterial activity of ZnO nanoparticles. *Mater. Res. Bull.* **76**, 48–61 (2016).
55. Hefnawy, M. A., Medany, S. S., El-Sherif, R. M., El-Bagoury, N. & Fadlallah, S. A. High-performance IN738 superalloy derived from turbine blade waste for efficient ethanol, ethylene glycol, and urea electrooxidation. *J. Appl. Electrochem.* <https://doi.org/10.1007/s10800-023-01862-7> (2023).
56. Hefnawy, M. A., Medany, S. S., El-Sherif, R. M. & Fadlallah, S. A. NiO-MnOx/polyaniline/graphite electrodes for urea electrocatalysis: Synergetic effect between polymorphs of MnOx and NiO. *ChemistrySelect* **7**, e202103735. <https://doi.org/10.1002/slct.202103735> (2022).
57. Al-Kadhi, N. S. *et al.* Polyaniline-supported nickel oxide flower for efficient nitrite electrochemical detection in water. *Polymers (Basel)* **15**, 1804. <https://doi.org/10.3390/polym15071804> (2023).
58. Xie, J. & Xie, Y. Transition metal nitrides for electrocatalytic energy conversion: Opportunities and challenges. *Chem. Eur. J.* **22**, 3588–3598 (2016).
59. Tian, G. *et al.* Nitrogen-doped graphene/carbon nanotube hybrids: In situ formation on bifunctional catalysts and their superior electrocatalytic activity for oxygen evolution/reduction reaction. *Small* **10**, 2251–2259 (2014).
60. Eliwa, A. S. *et al.* Ultrasonic-assisted synthesis of nickel metal-organic framework for efficient urea removal and water splitting applications. *Synth. Met.* **294**, 117309. <https://doi.org/10.1016/j.synthmet.2023.117309> (2023).
61. Subbaraman, R. *et al.* Trends in activity for the water electrolyser reactions on 3 d M (Ni Co, Fe, Mn) hydr (oxy) oxide catalysts. *Nat. Mater.* **11**, 550–557 (2012).
62. Kumar, S. *et al.* Grapefruit juice containing rich hydroxyl and oxygenated groups capable of transforming 1D structure of NiCo<sub>2</sub>O<sub>4</sub> into 0D with excessive surface vacancies for promising energy conversion and storage applications. *J. Energy Storage* **68**, 107708 (2023).
63. Laghari, A. J. *et al.* Surface modification of Co<sub>3</sub>O<sub>4</sub> nanostructures using wide range of natural compounds from rotten apple juice for the efficient oxygen evolution reaction. *Int. J. Hydrog. Energy* **48**, 15447–15459 (2023).
64. Gardner, G. *et al.* Structural basis for differing electrocatalytic water oxidation by the cubic, layered and spinel forms of lithium cobalt oxides. *Energy Environ. Sci.* **9**, 184–192. <https://doi.org/10.1039/C5EE02195B> (2016).
65. Song, F. & Hu, X. Exfoliation of layered double hydroxides for enhanced oxygen evolution catalysis. *Nat. Commun.* **5**, 4477 (2014).
66. Li, M. *et al.* Facile synthesis of electrospun MFe<sub>2</sub>O<sub>4</sub> (M = Co, Ni, Cu, Mn) spinel nanofibers with excellent electrocatalytic properties for oxygen evolution and hydrogen peroxide reduction. *Nanoscale* **7**, 8920–8930 (2015).
67. Tahira, A. *et al.* Facile deposition of palladium oxide (PdO) nanoparticles on CoNi<sub>2</sub>S<sub>4</sub> microstructures towards enhanced oxygen evolution reaction. *Nanotechnology* **33**, 275402 (2022).
68. Solangi, M. Y. *et al.* An efficient palladium oxide nanoparticles@Co<sub>3</sub>O<sub>4</sub> nanocomposite with low chemisorbed species for enhanced oxygen evolution reaction. *Int. J. Hydrog. Energy* **47**, 3834–3845. <https://doi.org/10.1016/j.ijhydene.2021.11.042> (2022).

69. Hanan, A. *et al.* Co<sub>2</sub>FeO<sub>4</sub>@rGO composite: Towards trifunctional water splitting in alkaline media. *Int. J. Hydrog. Energy* **47**, 33919–33937. <https://doi.org/10.1016/j.ijhydene.2022.07.269> (2022).
70. Chang, J. *et al.* Nitrogen-doped porous carbon encapsulated nickel iron alloy nanoparticles, one-step conversion synthesis for application as bifunctional catalyst for water electrolysis. *Electrochim. Acta* **389**, 138785. <https://doi.org/10.1016/j.electacta.2021.138785> (2021).
71. Yan, X., Tian, L. & Chen, X. Crystalline/amorphous Ni/NiO core/shell nanosheets as highly active electrocatalysts for hydrogen evolution reaction. *J. Power Sources* **300**, 336–343. <https://doi.org/10.1016/j.jpowsour.2015.09.089> (2015).
72. Yu, M. *et al.* A hierarchically porous and hydrophilic 3D nickel–iron/MXene electrode for accelerating oxygen and hydrogen evolution at high current densities. *Nano Energy* **63**, 103880. <https://doi.org/10.1016/j.nanoen.2019.103880> (2019).
73. Mugheri, A. Q. *et al.* Facile efficient earth abundant NiO/C composite electrocatalyst for the oxygen evolution reaction. *RSC Adv.* **9**, 5701–5710 (2019).
74. Xie, M. *et al.* An Fe (TCNQ)<sub>2</sub> nanowire array on Fe foil: An efficient non-noble-metal catalyst for the oxygen evolution reaction in alkaline media. *Chem. Commun.* **54**, 2300–2303 (2018).
75. Faid, A. Y., Barnett, A. O., Seland, F. & Sunde, S. Ni/NiO nanosheets for alkaline hydrogen evolution reaction: In situ electrochemical-Raman study. *Electrochim. Acta* **361**, 137040. <https://doi.org/10.1016/j.electacta.2020.137040> (2020).
76. Liu, T., Sun, X., Asiri, A. M. & He, Y. One-step electrodeposition of Ni–Co–S nanosheets film as a bifunctional electrocatalyst for efficient water splitting. *Int. J. Hydrog. Energy* **41**, 7264–7269. <https://doi.org/10.1016/j.ijhydene.2016.03.111> (2016).

## Acknowledgements

We extend our sincere appreciations to Researchers Supporting Project number (RSP2024R79), King Saud University, Riyadh, Saudi Arabia, for partial funding of this work.

## Author contributions

Conception and design of study: S.S.M., A.N., M.A.H., R.A.S. Acquisition of data: M.A.H., A.N., S.S.M.. Analysis and interpretation of data: M.A.H., S.S.M. Drafting the manuscript: M.A.H., S.S.M. Revising the manuscript critically for important intellectual content: A.N., R.A.S.

## Competing interests

The authors declare no competing interests.

## Additional information

**Correspondence** and requests for materials should be addressed to S.S.M. or M.A.H.

**Reprints and permissions information** is available at [www.nature.com/reprints](http://www.nature.com/reprints).

**Publisher's note** Springer Nature remains neutral with regard to jurisdictional claims in published maps and institutional affiliations.



**Open Access** This article is licensed under a Creative Commons Attribution 4.0 International License, which permits use, sharing, adaptation, distribution and reproduction in any medium or format, as long as you give appropriate credit to the original author(s) and the source, provide a link to the Creative Commons licence, and indicate if changes were made. The images or other third party material in this article are included in the article's Creative Commons licence, unless indicated otherwise in a credit line to the material. If material is not included in the article's Creative Commons licence and your intended use is not permitted by statutory regulation or exceeds the permitted use, you will need to obtain permission directly from the copyright holder. To view a copy of this licence, visit <http://creativecommons.org/licenses/by/4.0/>.

© The Author(s) 2024